Crystallographically oriented Co and Ni nanocrystals inside ZnO formed by ion implantation and postannealing

Shengqiang Zhou,* K. Potzger, J. von Borany, R. Grötzschel, W. Skorupa, M. Helm, and J. Fassbender
Institute of Ion Beam Physics and Materials Research, Forschungszentrum Dresden-Rossendorf, P.O. Box 510119, 01314 Dresden, Germany

(Received 24 September 2007; revised manuscript received 19 November 2007; published 24 January 2008)

In the last decade, transition-metal-doped ZnO has been intensively investigated as a route to room-temperature diluted magnetic semiconductors (DMSs). However, the origin for the reported ferromagnetism in ZnO-based DMS remains questionable. Possible options are diluted magnetic semiconductors, spinodal decomposition, or secondary phases. In order to clarify this question, we have performed a thorough characterization of the structural and magnetic properties of Co- and Ni-implanted ZnO single crystals. Our measurements reveal that Co or Ni nanocrystals (NCs) are the major contribution of the measured ferromagnetism. Already in the as-implanted samples, Co or Ni NCs have formed and they exhibit superparamagnetic properties. The Co or Ni NCs are crystallographically oriented with respect to the ZnO matrix. Their magnetic properties, e.g., the anisotropy and the superparamagnetic blocking temperature, can be tuned by annealing. We discuss the magnetic anisotropy of Ni NCs embedded in ZnO concerning the strain anisotropy.

DOI: 10.1103/PhysRevB.77.035209 PACS number(s): 75.50.Pp, 71.55.Gs, 75.75.+a, 61.05.cp

I. INTRODUCTION

Recently, diluted magnetic semiconductors (DMSs) have been under intensive investigation due to their potential applications in spintronics. In DMS materials, transition or rare-earth metal ions are substituted onto cation sites and are coupled with free carriers to yield ferromagnetism via indirect interaction. Mn-doped InAs (Ref. 1) and GaAs (Ref. 2) are the best studied DMS materials. Conventional III-V semiconductors are widely used for high-speed electronic and optoelectronic devices. The discovery of hole-mediated ferromagnetism in (Ga,Mn)As opened the way to integrate spin-based phenomena into mainstream microelectronics and optoelectronics as well as taking advantage of already established fabrication processes. Electrically controlled spintronic devices based on GaMnAs and InMnAs have been successfully designed and tested at low temperatures, e.g., a spin light emitting diode using GaMnAs as a spin injector.[3] However, the highest Curie temperature (T_C) reported in (Ga,Mn)As is ~170 K,[4] which is far below room temperature and limits its regular application.

In 2000, Dietl *et al.*[5] used a mean field theory to estimate the ordering temperature T_C of ferromagnetic semiconductors, and they predict that room-temperature ferromagnetism can be created by substituting Mn ions in *p*-type wide-band-gap semiconductors such as GaN and ZnO. Sato and Katayama-Yoshida calculated the properties of *n*-type ZnO doped with 3*d* transition metal (TM) ions (V, Cr, Mn, Fe, Co, and Ni).[6] The ferromagnetic state, with a T_C of around 2000 K, is predicted to be favorable for V, Cr, Fe, Co, and Ni in ZnO, while Mn-doped ZnO is predicted to be antiferromagnetic. These predictions largely boosted intensive experimental activities on transition-metal-doped GaN and ZnO. A large number of research groups have reported the experimental observation of ferromagnetism in (from Sc to Ni) TM-doped ZnO (Refs. 7–15) fabricated by various methods including ion implantation. For a comprehensive review, see Refs. 16–18. However, in these reports, the magnetic properties using the same dopant vary considerably. For example, the saturation moment and Curie temperature for Mn-doped ZnO ranges from $0.075\mu_B$/Mn, 400 K,[9] to $0.17\mu_B$/Mn, 30–45 K,[12] respectively. In contrast to these publications, other groups reported the observation of antiferromagnetism,[19–21] spin-glass behavior,[22,23] and paramagnetism[20,24–26] in TM-doped ZnO. Recently, it was also found that nanoscale precipitates can contribute to the ferromagnetic properties substantially.[27–34]

Publications claiming the intrinsic ferromagnetism in TM-doped ZnO are often based solely on magnetization measurements using high sensitivity superconducting quantum interference device magnetometry (SQUID) and structure characterizations using laboratory-equipped x-ray diffraction. The latter has been demonstrated to be not sensitive enough to detect nanoscale precipitates.[28] Nowadays, the research community puts more effort into judging if TM ions in semiconductors are homogenously distributed and if the ferromagnetism is intrinsic.[35,36] Anomalous Hall effect (AHE), which verifies charge carrier participation in the magnetic order, has been suggested to judge about carrier-mediated ferromagnetism arising from DMS. However, a recent study presents the co-occurrence of superparamagnetism and AHE in Co-doped TiO_2 films.[37] Another criterion is the magnetic anisotropy[15,38,39] as a signature of the intrinsic ferromagnetism. The controversy in the magnetic properties of ZnO-based DMS, as stated above, might partially be due to the insufficient characterization of the samples.[40–42] Particularly, a careful correlation between structure and magnetism should be established by sophisticated methods. Synchrotron radiation based x-ray diffraction (SR-XRD) is a powerful tool to detect small precipitates, e.g., metallic TM nanocrystals in ZnO.[28] On the other hand, element selective measurements of the magnetic properties, e.g., x-ray magnetic circular dichroism (XMCD)[43] and Mössbauer spectroscopy,[28,32] address the origin of the measured magnetism directly.

The present work is devoted to a comprehensive investigation of Co- and Ni-doped ZnO. By SR-XRD and SQUID

magnetometry, we correlate the structural and magnetic properties. We attempt to answer the following questions concerning the presence of ferromagnetic precipitates.

(1) How do the crystalline precipitates orient with respect to the host matrix?

(2) Which techniques are suitable to detect these precipitates?

(3) Are these precipitates the major contribution of the measured ferromagnetism or is there another source which contributes?

(4) Can these nanoscale precipitates exhibit magnetic properties, e.g., magnetic anisotropy, concerning the criteria above mentioned?

(5) How do these precipitates behave upon thermal annealing?

The paper is organized as follows. In Sec. II, all the experimental methods employed will be described. Then, the results will be presented in two sections. In Sec. III, we will focus on the as-implanted samples and discuss the orientation, the superparamagnetism, and the magnetic anisotropy of Co and Ni NCs. In Sec. IV, we will describe the structure and magnetism evolution due to high vacuum annealing. Finally, in Sec. V, we discuss the origin of the magnetic anisotropy for the oriented Co, Ni NCs system and the possible formation of Co/CoO and Ni/NiO core/shell structures upon annealing at 923 K. This paper is concluded in Sec. VI.

II. EXPERIMENTS

Commercial ZnO single crystals grown by the hydrothermal method were implanted with Co or Ni ions at 623 K with a fluence ranging from 0.8×10^{16} to 8×10^{16} cm^{-2}. The implantation energy was 180 keV, which resulted in a projected range of $R_P=89\pm29$ nm and a maximum atomic concentration from ~1% to ~10% (TRIM code[44]). Thermal annealing was performed in a high vacuum ($<10^{-6}$ mbar) furnace from 823 to 1073 K.

The lattice damage induced by implantation was evaluated by Rutherford backscattering/channeling spectrometry (RBS/C). RBS/C spectra were collected with a collimated 1.7 MeV He^+ beam at a backscattering angle of 170°. The sample was mounted on a three-axis goniometer with a precision of 0.01°. During channeling measurement, the sample was aligned to make the ZnO⟨0001⟩ axis parallel to the impinging He^+ beam. χ_{min}, the channeling minimum yield in RBS/C, is the ratio of the backscattering yield at channeling condition to that for a random beam incidence.[45] Therefore, χ_{min} labels the degree of lattice disorder upon implantation and an amorphous sample shows a χ_{min} of 100%, while a perfect single crystal corresponds to a χ_{min} of 1%–2%.

Magnetic properties were measured with a SQUID (Quantum Design MPMS) magnetometry. The samples were measured with the field along both the in- and out-of-plane directions. We studied both the temperature dependence of the magnetization at a constant field and the field dependence at a constant temperature. By SQUID, virgin ZnO is found to be purely diamagnetic with a susceptibility of -2.65×10^{-7} emu/Oe g. This background has been subtracted from the magnetic data. The temperature dependent magnetization measurement has been carried out in the following way. The sample was cooled in zero field from above room temperature to 5 K. Then, a 50 Oe field was applied and the zero field cooled magnetization curve (ZFC curve) was measured with increasing temperature from 5 to 350 K, after which the field cooled magnetization curve (FC curve) was measured in the same field from 350 to 5 K with decreasing temperature.

Structural analysis was performed both by SR-XRD and conventional XRD. SR-XRD was performed at the Rossendorf beamline (BM20) at the ESRF with an x-ray wavelength of 0.154 nm. Conventional XRD was performed with a Siemens D5005 equipped with a Cu-target source. In XRD measurement, we use $2\theta-\theta$ scans to identify crystalline precipitates and pole figures (azimuthal ϕ scan) for determining their crystallographical orientation. As a standard approach, for an XRD ϕ scan, one first tilts the sample by the angle of χ from the sample surface (χ is the angle between the diffraction plane of interest and the sample surface) and fixes the Bragg angle. Subsequently, the spectrum is recorded during azimuthal rotation with respect to the sample normal. The pole figure is constructed by a series of ϕ scans at different χ.

III. AS-IMPLANTED SAMPLES

A. ZnO lattice damage upon implantation

RBS/C is used to check the lattice damage after implantation. Figure 1 shows RBS/C spectra for different fluences. The arrow labeled Zn indicates the energy for backscattering from surface Zn atoms. The implanted Co or Ni ions cannot be detected for the very low fluence (0.8×10^{16} cm^{-2}, not shown). However, they are more pronounced as a hump in the random spectrum for larger fluences of 4×10^{16} and 8×10^{16} cm^{-2} (not shown). The humps in the channeling spectra mainly originate from the lattice disordering due to implantation. As expected, $\chi_{\min}$ increases with increasing fluence (see Table I). Note that the highest Co fluence induced comparable lattice damage with the middle fluence and less than the damage created by the same fluence of Ni. The reason could be a dopant specific self-annealing process.[46] RBS/C measurements also reveal that the ZnO is a hard material with respect to irradiation. The host material still partly remains in a crystalline state after irradiation with Co and Ni ions up to a fluence of 8×10^{16} cm^{-2} (χ_{min} of 59% and 69%, respectively).

B. Crystallographically oriented Co and Ni nanocrystals

SR-XRD is used to identify the precipitates in ZnO after Co or Ni implantation. Figure 2 shows the XRD $2\theta-\theta$ scans for all samples implanted with different fluences. At a low fluence (0.8×10^{16} cm^{-2}), no crystalline Co or Ni NCs could be detected. At a fluence of 4×10^{16} cm^{-2}, the hcp-Co(0002) [or fcc-Co(111)] and Ni(111) peak appear, respectively, and grow with increasing fluence. The full width at half maximum (FWHM) of the Co or Ni peak decreased with fluence, indicating the growth of the average diameter of these NCs

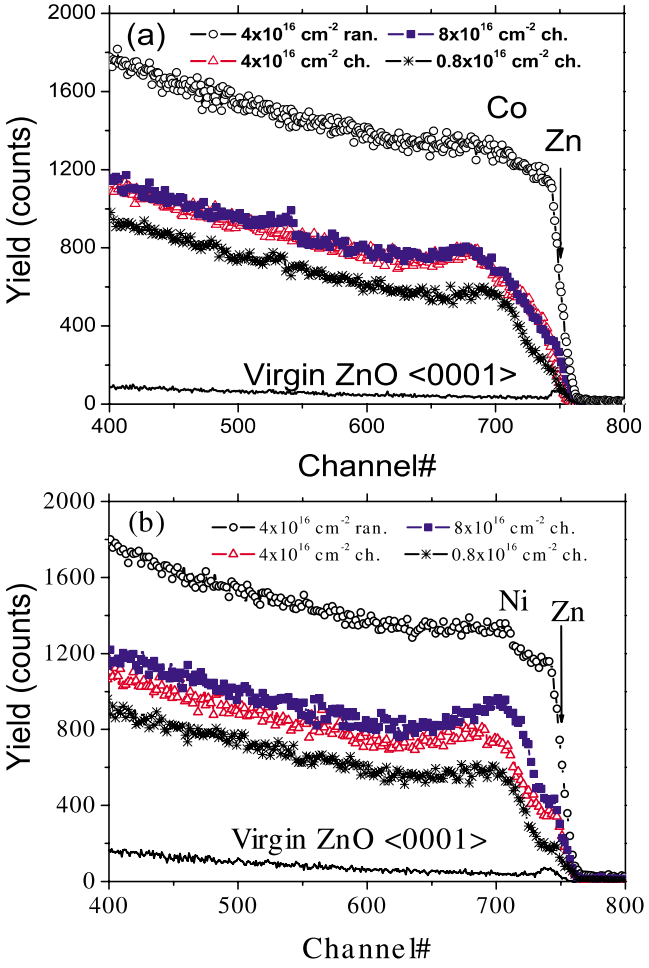

FIG. 1. (Color online) RBS random (ran.) and channeling (ch.) spectra: (a) Co implanted ZnO and (b) Ni-implanted ZnO (the fluence for Co and Ni ions is indicated). The yield of channeling spectra progressively decreases with increasing fluence.

(Table I). The crystallite size is calculated using the Scherrer formula,[47]

$$d = 0.9\lambda/(\beta \cos \theta), \quad (1)$$

where λ is the wavelength of the x ray, θ the Bragg angle, and β the FWHM of 2θ in radians.

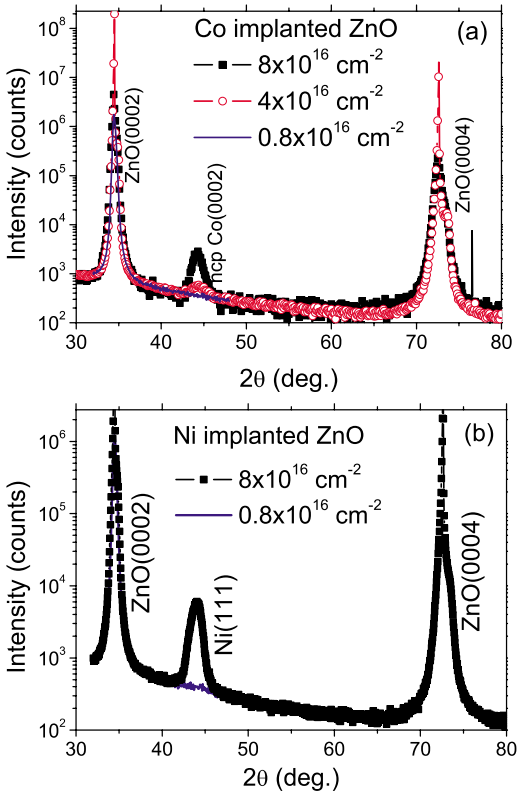

FIG. 2. (Color online) SR-XRD $2\theta-\theta$ scan revealing the existence of Co or Ni precipitates in (a) Co-implanted ZnO and (b) Ni-implanted ZnO.

Note that there is only one peak for Co or Ni detectable, which indicates that the crystallites of Co or Ni are highly oriented with respect to the host matrix. The surface orientation is hcp-Co(0001) [or fcc-Co(111)]‖ZnO(0001) and fcc-Ni(111)‖ZnO(0001), respectively.

The Co hcp structure only differs in the stacking from the fcc one. Since the Bragg angles (θ) for hcp-Co(0002) (θ =22.38°) and fcc-Co(111) (θ=22.12°) are rather close to each other, it is difficult to assign these peaks in Fig. 2(a) to hcp-Co or fcc-Co. A ϕ scan or pole figure on one of the diffraction planes not parallel with the sample surface (i.e., tilted by an angle χ from sample surface) helps to identify

TABLE I. Structural and magnetic properties for Co- and Ni-implanted ZnO with different fluences. Metallic Co/Ni fraction corresponds to the percentage of metallic Co/Ni compared with all implanted Co/Ni.

Fluence (cm^{-2})	χ_{min} (RBS/C)	Crystallite size (XRD) (nm)	Saturation magnetization[a] (μ_B/Co or /Ni)	Metallic fraction	Coercivity[a] (Oe)	T_B (K)	Crystallite size[b] (nm)
Co: 0.8×10^{16}	44%						
Co: 4×10^{16}	54%	5	0.29 (5 K)	17%	1400 (5 K)	45	4.3
Co: 8×10^{16}	57%	8	0.44 (5 K)	26%	1400 (5 K)	300	8.1
Ni: 0.8×10^{16}	45%		0.05 (10 K)	8%	10 (10 K)	≤5	<9.4
Ni: 4×10^{16}	57%	6	0.16 (10 K)	27%	30 (10 K)	16	14
Ni: 8×10^{16}	69%	8	0.22 (10 K)	37%	120 (10 K)	70	23

[a]Refer to the easy axis at a saturation field of 10000 Oe for Co-ZnO and 1500 Oe for Ni-ZnO.
[b]Calculation from the average blocking temperature by Eq. (2).

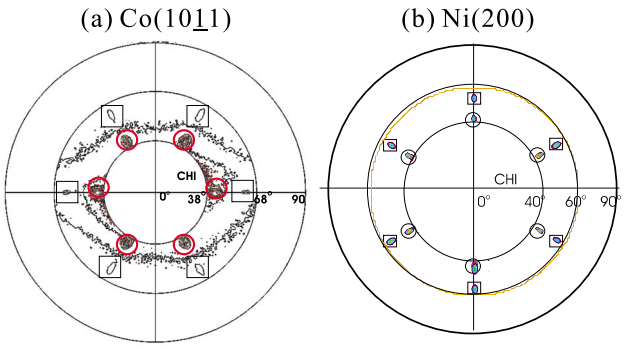

FIG. 3. (Color online) XRD pole figure revealing the crystallographical orientation relationship between Co/Ni NCs and ZnO matrix. (a) Co(10$\underline{1}$1) (in square) together with the tail of ZnO(10$\underline{1}$2) (in circle). The data points out of squares and circles are due to the background. (b) Ni(200) (in square) together with the tail of ZnO(10$\underline{1}$2) (in circle).

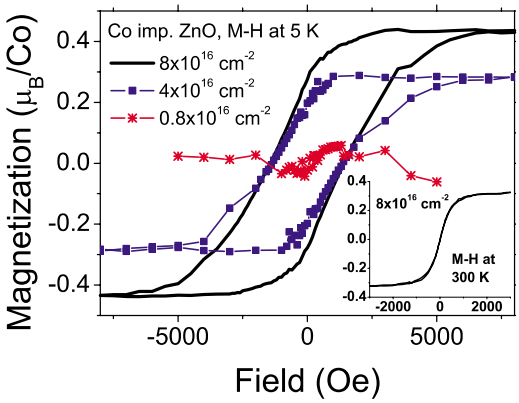

FIG. 4. (Color online) Hysteresis loops measured at 5 K for Co-implanted ZnO with different fluences (for the sample with the fluence of 0.8×10^{16} cm^{-2} only a half loop is shown). Inset: hysteresis loop measured at 300 K for the sample with the highest fluence.

hcp- or fcc-Co NCs and also reveals the crystallographical orientation relationship. By this approach, we find that only hcp-Co is present in the as-implanted samples. Figures 3(a) and 3(b) show the pole figure of hcp-Co(10$\underline{1}$1) and Ni(200), respectively. The radial coordinate is the angle (χ) by which the surface is tilted out of the diffraction plane. The azimuthal coordinate (ϕ) is the angle of rotation about the surface normal. The pole figure shows poles of hcp-Co(10$\underline{1}$1) at $\chi\sim61.9°$ and Ni(200) at $\chi\sim54.8°$. Both exhibit a sixfold symmetry. Since ZnO(10$\underline{1}$2) and hcp-Co(10$\underline{1}$1) have similar Bragg angle, the poles of ZnO(10$\underline{1}$2) also show up at $\chi\sim42.8°$ with much more intensities. The results are consistent with the theoretical Co(10$\underline{1}$1) pole figure viewed along [0001] and Ni(200) pole figure viewed along the [111] direction. Therefore, we can conclude that these Co and Ni NCs are crystallographically oriented with respect to the ZnO matrix. The in-plane orientation relationship is hcp-Co[10$\underline{1}$0]$\|$ZnO[10$\underline{1}$0] and Ni[112]$\|$ZnO[10$\underline{1}$0]. Due to the hexagonal structure of Co and sixfold symmetry of Ni viewed along the [111] direction, it is not difficult to understand their crystallographical orientation onto hexagonal ZnO.

At this point, we have to remind the reader that in our former work on Ni-implanted ZnO, the XRD measurement was performed on a conventional laboratory-equipped diffractometry (CXRD).[29] CXRD reveals similar results as SR-XRD (from the Ni fluence of 4×10^{16} cm^{-2}, Ni NCs start to form). However, CXRD fails to detect Fe NCs in ZnO,[28] where Fe NCs are not well oriented like the case of Ni in ZnO. The peak intensity in XRD is proportional to the diffraction volume, i.e., the number of diffraction planes which are parallel to each other. For a $2\theta-\theta$ scan, the crystallographic orientation results in much more diffraction volume than the random orientation. Therefore, the highly ordered orientation of NCs makes them easier to detect. As expected, Co NCs are also detectable in the CXRD measurement (not shown).

C. Magnetic properties of Co and Ni nanocrystals

The magnetic properties of Co- and Ni-implanted ZnO were measured by SQUID magnetometry with the field parallel and perpendicular to the sample surface. Co-implanted samples exhibit a hard axis parallel to the sample surface, while the easy axis is perpendicular to the surface. For Ni-implanted samples, the anisotropy directions are reversed. In this section, we investigate the superparamagnetism of the implanted ZnO samples and their magnetic anisotropy.

1. Superparamagnetic Co and Ni nanocrystals

From the XRD results, we know that Co and Ni NCs have been formed in the as-implanted samples. For magnetic nanoparticles, the formation of domain walls is energetically unfavorable. Below a certain size (typically in the range of 15–30 nm depending on the material), the particle stays in a single-domain configuration. If the particle size is sufficiently small, above a particular temperature (so-called blocking temperature, T_B), thermal fluctuations dominate and no preferred magnetization direction can be defined. Such a system of superparamagnetic particles does not exhibit a hysteresis curve above T_B; therefore, the coercivity (H_C) and the remanence (M_R) are both zero.

For a dc magnetization measurement in a small magnetic field by SQUID, T_B is given by

$$T_{B,SQUID}\approx\frac{K_{eff}V}{30k_B}, \tag{2}$$

where K_{eff} is the anisotropy energy density, V the particle volume, and k_B the Boltzmann constant.[48] For bulk crystals, $K_{\mathrm{eff}}(V)$ are 5.0×10^5 and 5.7×10^3 J m^{-3} for Co and Ni, respectively, at room temperature.

Phenomenologically, there are two characteristic features in the temperature dependent magnetization of a nanoparticle system. One is the irreversibility of the magnetization in a small applied field (e.g., 50 Oe) after ZFC and FC.[48] The other is the drastic drop of coercivity and remanence at a temperature close to or above T_B.[37]

Figure 4 shows the magnetization versus field reversal (M-H) measured at 5 K with the field applied perpendicular to the sample surface (along ZnO[0001]). A hysteretic behav-

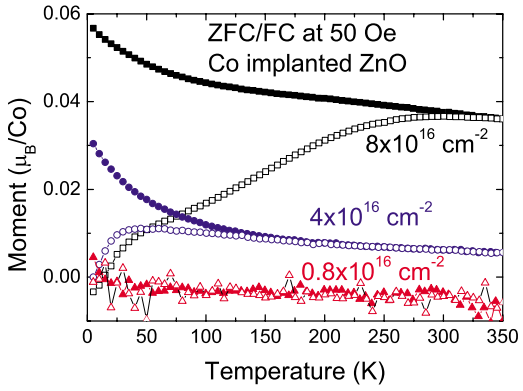

FIG. 5. (Color online) Magnetization curves at 50 Oe after ZFC (open symbol) and FC (solid symbol) for the Co-implanted ZnO. With increasing fluence, the Co NCs is growing in size, resulting in a higher blocking temperature.

ior is observed for the high-fluence implanted samples. A saturation behavior is also observed at 300 K for the sample with the highest fluence (Fig. 4, inset). However, neither coercivity nor remanence can be observed at 300 K. This is a strong indication for the superparamagnetism of a magnetic nanoparticle system. Knowing the formation of hcp-Co from XRD, it is reasonable to conclude that hcp-Co NCs are responsible for the magnetic behavior. For bulk hcp-Co crystals, the magnetic moment is 1.7 μ_B/Co at 0 K. Assuming the same value for Co NCs, around 17% and 26% of implanted Co ions are in the metallic state for the fluences of 4×10^{16} and 8×10^{16} cm^{-2}, respectively. Similar results are observed for Ni-implanted ZnO.[29]

Note that the hysteresis loop for the fluence of 4×10^{16} cm^{-2} exhibits two reversal steps. There is a very small kink when the field decreases from −2000 to −4000 Oe (and increases from 2000 to 4000 Oe). This wasp-waist shape of the loop is associated with magnetic phases with different coercivities.[31,49]

Temperature dependent magnetization with $H=50$ Oe was measured after ZFC and FC to confirm the superparamagnetism (Fig. 5). For the magnetic samples, a distinct difference in ZFC/FC curves is observed. ZFC curves show a gradual increase (deblocking) at low temperature and reach a broad peak, while FC curves continue to increase with decreasing temperature. The broad peaks in ZFC curves are due to the size distribution of Co NCs. In this paper, the temperature at the maximum of the ZFC curve is taken as the average blocking temperature (later referred as T_B). The ZFC/FC curves are general characteristics of magnetic nanoparticle systems with a broad size distribution.[50] T_B increases with the fluence, i.e., the size of nanoparticles. Table I lists the average size of Co NCs calculated by Eq. (1) (XRD) and Eq. (2) (SQUID). They are in a good agreement although there is also a size distribution in Co NCs.[51] The ZFC/FC magnetization was also measured for Ni-implanted samples.[29] Compared with Co, Ni has a much lower anisotropy energy density. For similar sizes of Ni NCs, the blocking temperature is therefore much lower than that of Co. Table I lists the average size of Ni NCs calculated by Eq. (1) (XRD) and Eq. (2) (SQUID). Although the trend is the same for both calculations, the values from SQUID are much larger than those from XRD data. One reason could be that the anisotropy energy density is underestimated by assuming the magnetocrystalline anisotropy constant. Another reason is that T_B is overestimated by taking the temperature at the maximum of the ZFC curve. According to the calculation by Farle,[51] and by Jacobsohn *et al.*,[52] the size dispersion for a given average particle diameter broadens the peak of ZFC curve and shifts it to higher temperatures.

2. Magnetic anisotropy

M-H loops were also measured for selective samples with Co fluence of 8×10^{16} cm^{-2} with the field both perpendicular and parallel to the sample surface. Figure 6(a) shows the comparison of the magnetization along ZnO[10$\underline{1}$0] and [0001] at 300 K. Figure 6(c) shows the orientation relationship between hcp-Co and ZnO and the measurement geometry. Obviously, Co[0001] is the easy axis, the same as a bulk hcp-Co crystal. The intersection of both curves gives an effective anisotropy field of 3000 Oe. At 5 K, the magnetic anisotropy is the same (not shown) and the coercivity of the easy axis is around 1400 Oe. The ratio between remanence and saturation magnetization is around 60%. This rather low remanence (below 100%) is due to the size distribution of nanomagnets. Very small nanomagnets behave superparamagnetically even at low temperatures and only have field induced magnetization. This is a rather universal feature for nanomagnets. For instance, in epitaxial MnAs nanoclusters in GaAs, the remanence is also below 100% along the easy axis.[53] Figure 6(b) shows the same measurement of Ni-implanted ZnO, while (d) shows the orientation relationship between fcc-Ni and ZnO and the measurement geometry. In contrast to bulk Ni where [111] is the easy axis, the easy axis is Ni[112] and the hard axis is Ni[111]. Moreover, as shown in Fig. 6(b), another in-plane direction Ni[110] is also an easy axis. Within the applied field, the magnetization curve along the hard axis does not intersect with that along the easy axis. The effective anisotropy field is much larger than 1500 Oe. This means that there are other contributions to the anisotropy dominating over the crystalline magnetic anisotropy. This will be discussed in Sec. V.

In the work by Norton *et al.*[27] epitaxial Co nanocrystals have been observed in Co-implanted ZnO single crystals. The nanocrystal size is estimated to be ~3.5 nm, which is below the superparamagnetic limit at room temperature. Therefore, the ferromagnetism above 300 K is very possible due to Co substitution onto the Zn site in the ZnO matrix. In our case, the measured superparamagnetism is well explained by the presence of Co and Ni nanocrystals. The formation of metallic nanocrystals already in the as-implanted state is due to the elevated implantation temperature (623 K), which facilitates the precipitation process. Implantation at low temperatures (e.g., 253 K) prohibits precipitation, however, it results in nonmagnetism in our case, e.g., Fe-implanted ZnO.[54]

IV. EFFECT OF POSTANNEALING

The postannealing was performed in high vacuum with temperatures ranging from 823 to 1073 K for 15 min. The

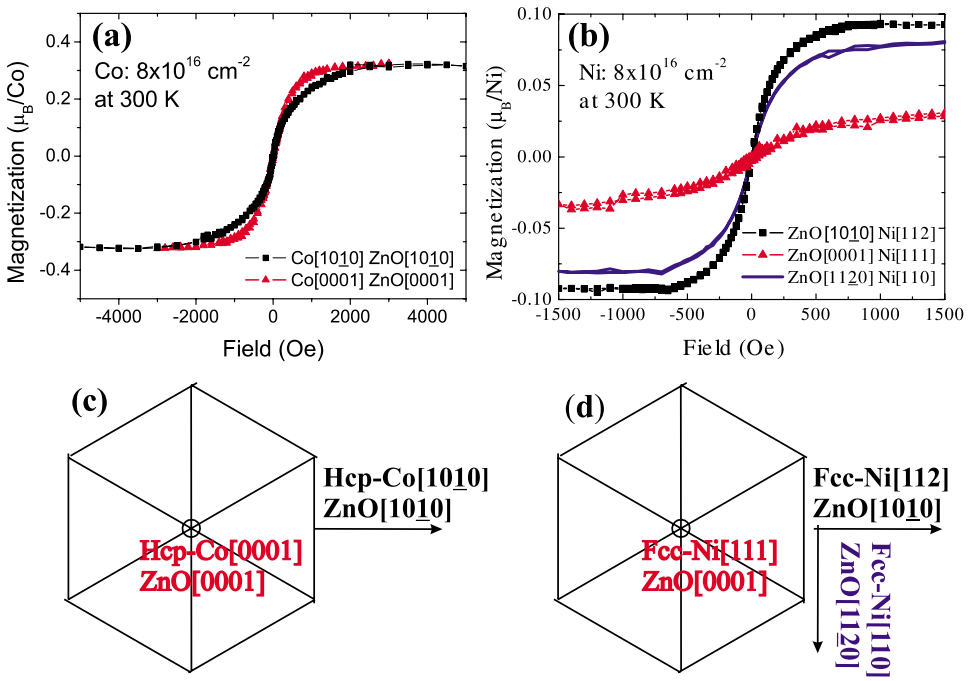

FIG. 6. (Color online) Hysteresis loops measured with the field along ZnO[0001] (out of plane) and [10$\bar{1}$0] (in plane) for Co/Ni-implanted ZnO with the fluence of 8×10^{16} cm^{-2} measured at 300 K. (a) Co-implanted ZnO and (b) Ni-implanted ZnO. (c) and (d) show the schematic geometry for magnetization measurements.

samples to be annealed were selected according to the SQUID measurement capability, namely, the temperature range from 1.8 to 400 K. Due to the higher anisotropy energy of Co, T_B in the ZFC curve of the highest fluence is already 300 K in the as-implanted state (see Fig. 5). The annealing is expected to increase the size of Co NCs and consequently increase T_B in the ZFC curve, which will exceed the temperature range of the SQUID magnetometry. Therefore, the sample implanted with the middle Co fluence was chosen. For Ni, the highest implantation fluence was chosen.

A. Lattice recovery

As shown in Fig. 1, ion implantation substantially induces lattice damage of ZnO crystals. Here, we show that this damage can be partially recovered by postannealing.

Figure 7 shows the RBS/C spectra for the sample implanted with a Co fluence of 4×10^{16} cm^{-2}. The annealing temperatures are given in the figure. With increasing annealing temperature, the channeling spectra indicate that the lattice disorder of ZnO progressively decreases. After annealing to 1073 K, the channeling spectrum is almost comparable to the virgin ZnO. Similar RBS/C results are observed for Ni-implanted ZnO upon annealing (not shown).

B. Evolution of structural properties

Figure 8(a) shows the development of Co NCs upon thermal annealing. The peak area and crystallite size calculated using the Scherrer formula[47] are compared in Table I. A broad scan [the inset of Fig. 8(a)] reveals only one peak from Co besides the ZnO peaks. An XRD ϕ scan has been used to distinguish between hcp- and fcc-Co (Fig. 9). We find only hcp-Co in the as-implanted sample and the sample annealed at 923 K, while both fcc- and hcp-Co are present in the sample annealed at 823 K. The broad peak in Fig. 8(a) (823 K ann.) is a superposition of hcp-Co(0002) and fcc-Co(111). The crystallographical orientation relationship between Co NCs and ZnO is hcp-Co(0001)[10$\bar{1}$0]||ZnO(0001)[10$\bar{1}$0]||fcc-Co(111)[112]. With this orientation, the 2θ-θ scans for hcp-Co(10$\bar{1}$1) and fcc-Co(200) are expected with a skew geometry at one of the azimuthal positions (e.g., at ϕ=0), as shown in Figs. 10(a) and 10(b), respectively. In skew geometry, the incident and the diffracted waves have the same angles to the surface, while the sample is tilted with respect to its surface normal. By this configuration, a noncoplanar, its surface normal does

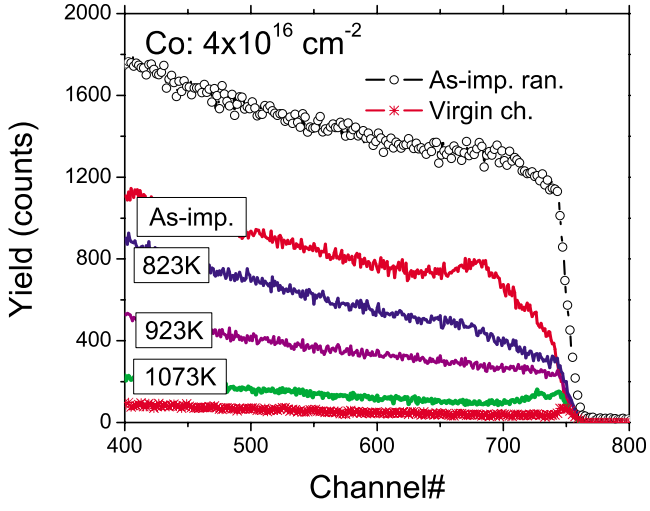

FIG. 7. (Color online) RBS random (ran.) and channeling (ch.) spectra for Co-implanted ZnO with a fluence of 4×10^{16} cm^{-2} after thermal annealing at different temperatures. The lattice damage induced by implantation is progressively reduced by increasing the annealing temperature.

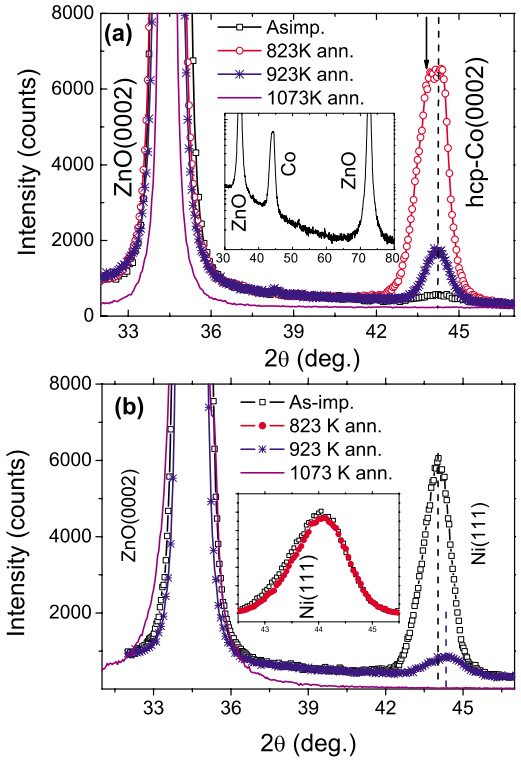

FIG. 8. (Color online) XRD 2θ-θ scans: (a) Co-implanted ZnO crystals with different annealing temperatures. The wide range XRD pattern for one of the samples (inset) reveals that no other crystalline phase (e.g., CoO) could be detected. The arrow points to the peak shoulder coming from the fcc-Co(111) diffraction in the sample of 823 K ann. (b) Ni-implanted ZnO crystals with different annealing temperatures. The inset shows a comparison between as-implanted and 823 K annealed samples.

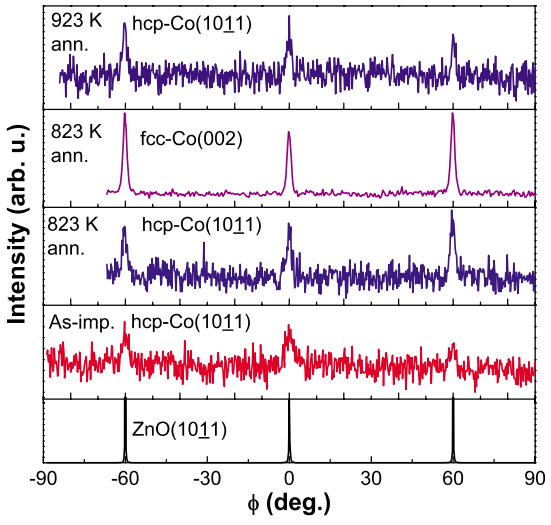

FIG. 9. (Color online) XRD ϕ scans for hcp-Co(10$\bar{1}$1) (θ =23.78° and $\chi\sim$61.9°), fcc-Co(002) (θ=25.76° and $\chi\sim$54.8°), and ZnO(10$\bar{1}$1) (θ=18.13° and $\chi\sim$61.6°) reveal the in-plane orientation relationship for Co NCs with respect to ZnO.

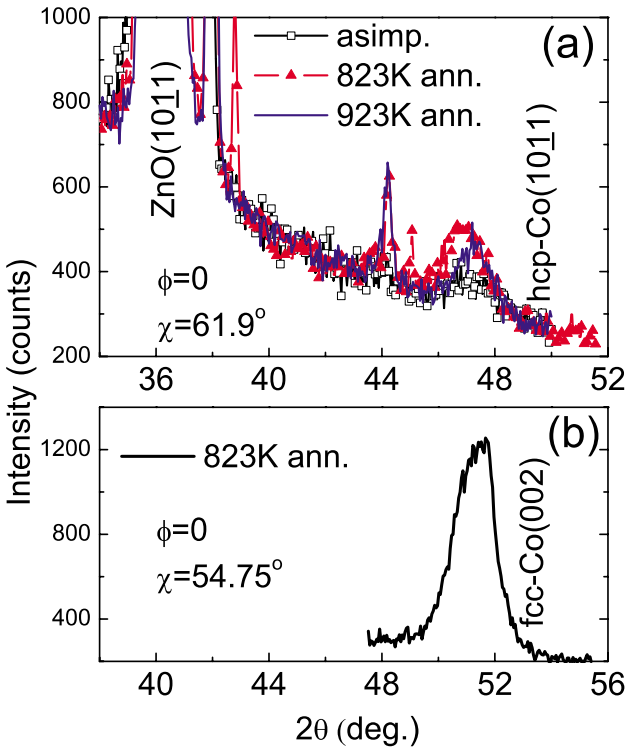

FIG. 10. (Color online) (a) 2θ-θ scans for ZnO(10$\bar{1}$1) and hcp-Co(10$\bar{1}$1); those small sharp peaks are from artificial noise in the measurements. (b) 2θ-θ scan for fcc-Co(002).

not lie in the plane defined by the incident and the diffracted waves, can be measured.[55] Note that the peak area of Co in Fig. 8, which is an approximate measure of the amount of Co NCs, increases drastically after 823 K annealing, while it decreases after 923 K annealing. It is reasonable to attribute this change to the formation and disappearance of fcc-Co. The fcc-Co is probably oxidized to the amorphous CoO after 923 K annealing, while finally the majority of Co NCs are oxidized to the amorphous state after annealing at 1073 K.

For Ni-implanted ZnO, the structure evolution upon annealing is similar, as shown in Fig. 8(b). The peak area and the crystallite size are listed in Table II. The mild temperature annealing (823 K) only slightly increases the grain size of Ni. The annealing at 923 K drastically decreases the peak area, while the grain size also decreases. Note that there is a significant shift in the Ni(111) peak (labeled by dashed lines), which indicates the relaxation of lattice strain. After annealing at 1073 K, the majority of Ni NCs could be oxidized to the amorphous state.

C. Evolution of magnetic properties

The structural phase transformation of Co NCs results in different magnetic properties as revealed by SQUID. Figure 11(a) shows the ZFC/FC magnetization curves for all samples annealed at different temperatures. Obviously, except for the sample annealed at 1073 K, the ZFC curves show a gradual increase (deblocking) at low temperature and reach a maximum at a temperature of T_B (shown in Table II),

TABLE II. Structural and magnetic properties for Co- and Ni-implanted ZnO with different fluences. Metallic Co/Ni fraction corresponds to the percentage of metallic Co/Ni compared with all implanted Co/Ni.

Sample	Peak area (XRD)	Crystallite size (XRD) (nm)	Saturation magnetization[a] (μ_B/Co or /Ni)	Metallic fraction	Coercivity[a] (Oe)	T_B (K)	Crystallite size[b] (nm)
Co: As-imp.	380	5	0.29 (at 10000 Oe)	17%	1400	45	4.3
Co: 823 K ann.	8330		0.36 (at 2000 Oe)	21%	250	80	5.2
Co: 923 K ann.	1400	10	0.32 (at 2000 Oe)	19%	450	330	8.3
Co: 1073 K ann.	0						
Ni: As-imp.	7312	8	0.22 (at 2000 Oe)	37%	230	70	<9.4
Ni: 823 K ann.	6590	9	0.22 (at 2000 Oe)	37%	200	80	14
Ni: 923 K ann.	750	7	0.18 (at 2000 Oe)	30%	220		
Ni: 1073 K ann.	0						

[a]Refer to the easy axis magnetization at 5 K at a saturation field as indicated.
[b]Calculation from the average blocking temperature by Eq. (2).

while FC curves continue to increase with decreasing temperature. No significant magnetization response is detected for the sample annealed at 1073 K. Note that T_B increases drastically above 330 K after annealing at 923 K. However, Jacobsohn *et al.*[56] reported a much lower T_B (250 K) of hcp-Co NCs with similar grain size (~10 nm). The higher T_B could be due to some other anisotropy energy, which stabilized the superparamagnetism at higher temperature. This will be discussed in Sec. V.

Hysteresis loops were measured for all samples in both parallel (ZnO[10$\bar{1}$0]||hcp-Co[10$\bar{1}$0]||fcc-Co[112]) and perpendicular (ZnO[0001]||hcp-Co[0001]||fcc-Co[111]) directions. Figures 11(b)–11(d) reveal that the anisotropy and coercivity can be tuned by different annealing procedures. The as-implanted sample only consists of hcp-Co NCs, which make the bulklike anisotropy persist along the [0001] direction with a high coercivity [Fig. 11(b)]. The sample annealed at 823 K mainly consists of fcc-Co with the easy axis along the fcc-Co[112] direction [Fig. 11(c)]. After annealing at 923 K, the sample shows an easy axis both along hcp-Co[10$\bar{1}$0] and hcp-Co[0001], but a higher coercivity along the latter direction. The magnetic properties of different samples are listed in Table II.

Figure 12 shows the magnetic properties of Ni-implanted ZnO upon annealing. As expected, the 823 K annealing increases T_B in the ZFC curve due to the increase of crystallite size. However, upon annealing at 923 K, the shape of ZFC magnetization curve deviates from others. There is no real

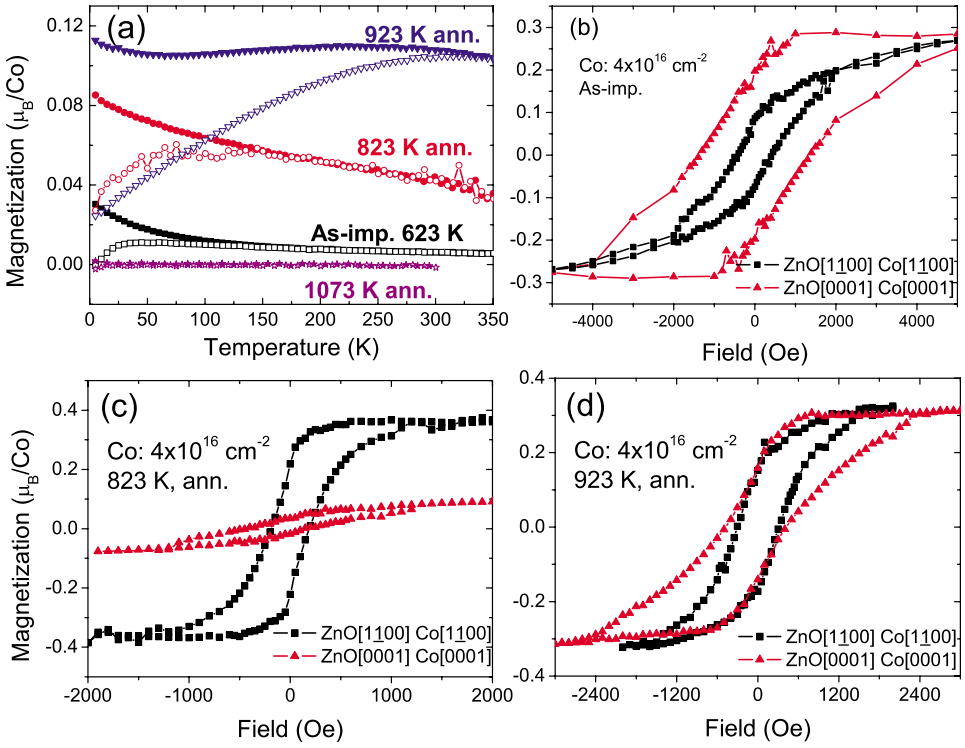

FIG. 11. (Color online) (a) ZFC/FC magnetization curves at 50 Oe for the samples after implantation and annealing at different temperatures. Solid symbols are FC curves, while open symbols are ZFC curves. [(b)–(d)] *M-H* curves measured at 5 K for all samples: along ZnO[10$\bar{1}$0]||hcp-Co[10$\bar{1}$0]||fcc-Co[112] (solid symbols) and ZnO[0001]||hcp-Co[0001]||fcc-Co[111] (open symbols). Implantation or annealing temperature is shown.

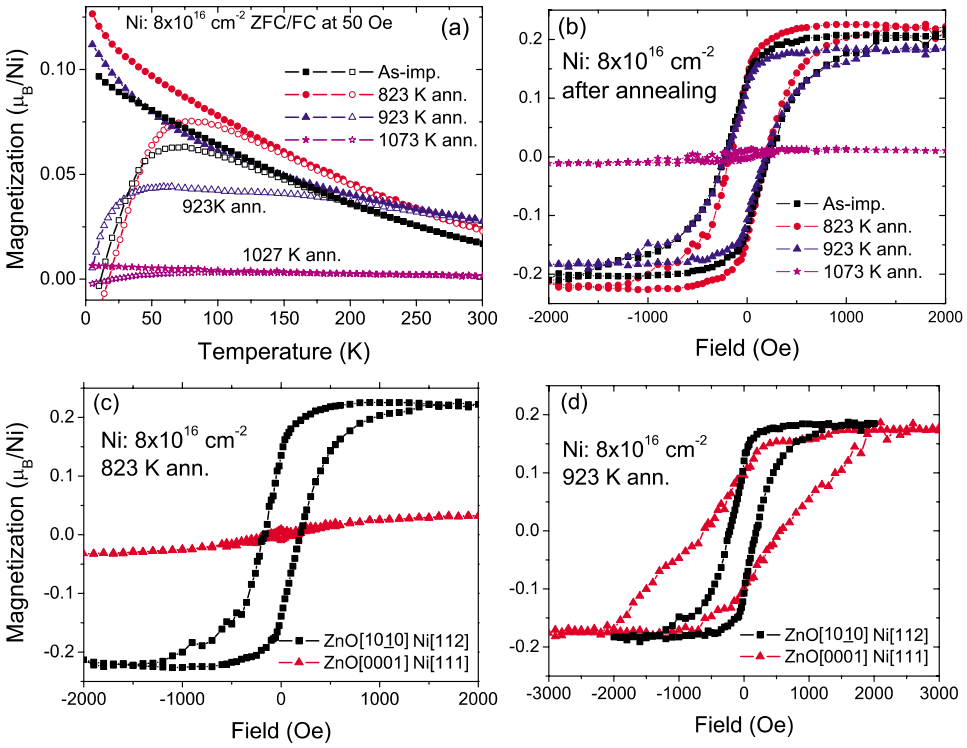

FIG. 12. (Color online) (a) ZFC/FC magnetization curves at 50 Oe for the samples after implantation and annealing at different temperatures. Solid symbols are FC curves, while open symbols are ZFC curves. (b) *M-H* curves measured at 5 K for all samples along ZnO[10$\bar{1}$0]‖fcc-Ni[112]. [(c) and (d)] *M-H* curves measured at 5 K for all samples along ZnO[10$\bar{1}$0]‖fcc-Ni[112] (solid symbols) and ZnO[0001]‖fcc-Co[111] (open symbols) after 823 and 923 K annealing, respectively. Implantation or annealing temperature is shown.

maximum but a broad plateau. The formation of Ni/NiO core/shell structure could introduce an exchange coupling, which contributes to another anisotropy energy. This will be discussed in the following section. Note that after annealing at 1073 K, the sample still exhibits a non-neglectful response in ZFC/FC magnetization measurement. There could be a small amount of Ni nanocrystals remaining, while they are beyond the detection limit in SR-XRD measurement.

V. DISCUSSION

A. Magnetic anisotropy of Co and Ni nanocrystals

As shown before, the magnetic anisotropy of Ni NCs embedded in ZnO is drastically different from bulk Ni. For bulk Ni, the magnetocrystalline anisotropy constant of K_1 is -5.7×10^3 J m^{-3} at 300 K. The [111] direction is the easy axis. For a single magnetic NC, the magnetocrystalline, shape, and magnetoelastic anisotropy have to be considered.

In principle, a uniformly magnetized single-domain spherical particle has no shape anisotropy because the demagnetizing factors are isotropic in all directions. However, in the case of a nonspherical sample, it will be easier to magnetize along a long axis than along a short one. The FWHM of the Ni peak in XRD 2θ-θ scans is a measure of the crystallite size. Along the Ni[111] direction, the crystallite size is estimated to be around 8 nm. For the in-plane direction, the crystallite size could be estimated by measuring a diffraction plane not parallel to the sample surface. We chose the Ni(200) diffraction plane. Figure 13 shows the comparison of the normalized Ni(111) and (200) peaks. Actually, Ni(200) is broader than (111), which means that the crystallite size along the in-plane direction is even smaller than the [111] direction. Therefore, the shape anisotropy is not the key reason to induce the easy axis along the in-plane direction.

Now, we consider the strain anisotropy. This kind of anisotropy is often described by a magnetoelastic energy term

$$k_{magnetoelastic} = -\tfrac{3}{2}\lambda_S \sigma \cos^2 \phi, \tag{3}$$

where λ_S is the magnetostriction constant, σ the stress, and ϕ the angle between the magnetization and the strain tensor axis.[57] The strain ϵ along the [111] direction of our Ni NCs can be calculated according to XRD measurement.

The lattice spacing is given by the Bragg law

$$2d_{expt} \sin\theta = \lambda, \tag{4}$$

where d_{expt} is the lattice spacing, θ the Bragg angle, and $\lambda = 0.154$ nm the wavelength of x ray. θ is obtained from Fig. 2. The strain is defined as follows:

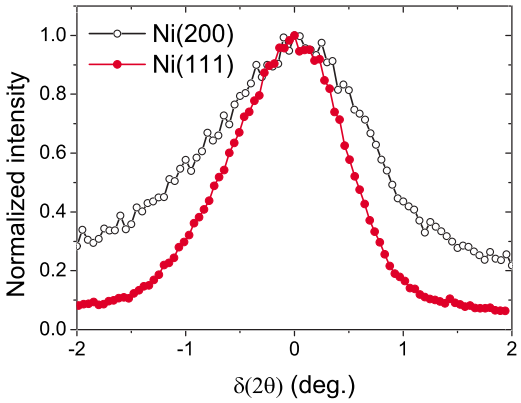

FIG. 13. (Color online) XRD 2θ-θ scan of Ni(200) and Ni(111).

TABLE III. Comparison of magnetic-anisotropy energy density: magnetocrystalline K_1 and magnetoelastic K_{ME}. λ_S is the magnetostriction coefficient, E the Young modulus, ϵ the elastic strain, and σ the stress ($\sigma = E\epsilon$).

Nanocrystals	k_{ME} (10^3 J m^{-3})	k_1 (10^3 J m^{-3})[a]	λ_S[a]	E (GPa)[a]	ϵ	σ (Gpa)
Ni (As-imp.)	54	−5.7	-24×10^{-6}	200	0.011	2.2
Ni (823 K ann.)	50	−5.7	-24×10^{-6}	200	0.010	2.0
Ni (923 K ann.)	25	−5.7	-24×10^{-6}	200	0.005	1.0
hcp-Co (As-imp.)	125	500	-5.5×10^{-5}	209	0.011	2.3

[a]Data from Refs. 58 and 59.

$$\epsilon = (d_{expt} - d)/d, \tag{5}$$

where d is the theoretical lattice spacing for bulk Ni or Co.

Using the approach and parameters in Refs. 58 and 59, the magnetoelastic anisotropy constant is calculated (see Table III). For Ni NCs, the magnetoelastic anisotropy constant is 1 order higher than the magnetocrystalline anisotropy constant. Therefore, the magnetoelastic anisotropy energy dominates the total anisotropy energy. This finding demonstrates the possibility to tune the magnetic properties by embedding magnetic NCs in different host matrices. The annealing at 823 K does not change the strain status significantly. After annealing up to 923 K, the elastic strain is partially released. However, the magnetoelastic anisotropy energy is still much higher than the magnetocrystalline one. Note the anisotropy change in Fig. 12(d) after 923 K annealing by comparing with the 823 K annealing. There could be another anisotropy source after 923 K annealing, which will be discussed in Sec. V B.

For hcp-Co, the magnetocrystalline anisotropy constant is very large, and it is difficult to be dominated by other anisotropy energy contribution (as shown in Table III). Therefore, the hcp-Co NCs in the as-implanted state still cause the bulklike anisotropy behavior to persist. However, the annealing at 823 K resulted in the coexistence of fcc-Co and hcp-Co NCs. Since fcc-Co is a metastable state, its magnetic and mechanic data are very limited. Therefore, in this paper, we will not discuss its magnetoelastic anisotropy energy. Nevertheless, fcc-Co[112] is the easy axis rather than [111], which could be due to the lattice strain, as the same reason for Ni nanocrystals in ZnO. After annealing at 923 K, hcp-Co is the only phase and the elastic strain is not significantly changed compared with the as-implanted state [see Fig. 8(a)]. However, the anisotropy is obviously changed. Like the Ni case, there could be another anisotropy source, which will be discussed in Sec. V B.

B. Annealing at 923 K

After annealing at 923 K, the magnetic properties, namely, ZFC/FC magnetization and magnetic anisotropy, are changed significantly compared with other samples. For the Co case, T_B in the ZFC curve increases drastically, while the FC curve is not monodecreased with increasing temperature. For the Ni case, there is a broad plateau in the ZFC curve.

One explanation for the higher T_B is the increase and broadening of the Co crystallite size. Jacobsohn *et al.* calculated the ZFC curves by varying different parameters, including the size distribution.[52] It is found that a slight broadening can result in a very broad and high ZFC curve. This can well explain the ZFC magnetization but not the FC magnetization. Moreover, the drastic changes in coercivity and magnetic anisotropy cannot be explained in such an approach. In addition, Table II lists the comparison of the XRD peak area and the magnetization upon annealing. Note that the XRD peak area decreases drastically by almost 1 order after 923 K annealing, which indicates the decreasing amount of the Co or Ni NCs; however, the saturation magnetization only decreases slightly.

Another explanation is related to other anisotropic energy contributions. Skumryev *et al.* have found that the exchange coupling between Co NCs and their CoO shells drastically increased the blocking temperature.[60] In our XRD measurement, the amount of metallic Co and Ni decreases after annealing at 923 K, which is very probably due to the oxidation. Therefore, we could assume the formation of a Co/CoO core/shell structure in our sample and the exchange coupling increases the blocking temperature. The exchange coupling is further confirmed by the vertical shift of the magnetization loop (Fig. 14). The loop curve is shifted along the magnetization axis after cooling from 350 K in an applied field.

The vertical shift of the magnetization loop is a strong evidence for the presence of an interfacial interaction be-

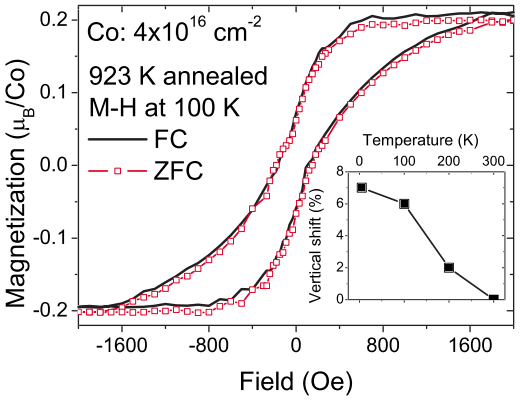

FIG. 14. (Color online) The sample annealed at 923 K shows a vertical shift along the magnetization axis after field cooling (H = 2000 Oe) due to the exchange coupling between FM and AFM materials. The field is along the ZnO[0001] direction. The inset shows the temperature dependence of the vertical shift.

tween an antiferromagnet (AFM) and a ferromagnet (FM),[61] i.e., the hcp-Co NCs are surrounded by CoO, which is amorphous, and therefore cannot be detected by XRD. Dobrynin *et al.*[61] presented a model to discuss the exchange coupling of nanoscaled Co/CoO core/shell structures. Below a critical size (12 nm) of Co cores, the interfacial exchange energy is larger than both the Zeeman energy of FM and the anisotropy energy of the AFM due to a large surface-to-volume ratio of NCs, and consequently some spins in the FM part can be frozen by the AFM part, leading to a vertical shift along the magnetization axis after field cooling. This model well explains our Co/CoO system with an average diameter of 10 nm for Co NCs. The vertical shift of the magnetization loop decreases with increasing temperature and disappears at a temperature between 200 and 300 K. This is consistent with the Néel temperature of 290 K for CoO.[60] Such a vertical shift is also observed in the FC loop measured along ZnO$[10\underline{1}0]\|$hcp-Co$[10\underline{1}0]$ (in plane) (not shown).

For the Ni-implanted sample annealed at 923 K, the hysteresis loop was also measured under both ZFC and FC conditions (not shown). A similar shift along the magnetization axis is observed. Therefore, we would assume the formation of a Co/CoO (Ni/NiO) core/shell structure. The exchange coupling between Co (Ni) and CoO (NiO) contributes another anisotropy energy. This explains the high blocking temperature and the change in magnetic anisotropy after annealing at 923 K.

Note that for both cases, the magnetization is only slightly decreased after annealing at 923 K. This is controversial with the drastic decrease of the diffraction intensity (see Fig. 8). One possible reason is the formation of small Co or Ni nanocrystals due to annealing. As shown in Table I, only around 10%–40% of Co or Ni forms as metallic nanocrystals and others remain as dispersed ones. Annealing at 923 K, on one hand, oxidized some metallic nanocrystals partially, and, on the other hand, could induce the gettering of dispersed Co and Ni and result in small metallic nanocrystals. Below a critical size, nanocrystals are nondetectable by XRD. Another reason could be that only a thin shell of Co or Ni nanocrystals transforms into oxides, which results in the invisibility of oxides in XRD even if they are crystalline. Obviously, a detailed investigation using transmission electron microscopy or other more sensitive techniques should be performed to clarify this controversy.

VI. CONCLUSIONS

A thorough characterization of the structural and magnetic properties has been presented on Co- and Ni-implanted ZnO single crystals. The results by SR-XRD and SQUID magnetometry correlate well with each other. The major conclusions are summarized as follows.

(1) Co or Ni NCs have been formed in ZnO upon ion implantation. Their crystalline sizes, generally below 10 nm, increase with increasing fluence. Implanted Co or Ni is in metallic states from several percent to 37%, while the remaining could be diluted into the ZnO matrix. The Co or Ni NCs are the origin of the measured ferromagnetism.

(2) The Co and Ni NCs are crystallographically oriented with respect to ZnO host matrix. The orientation relationship is as follows: hcp-Co$(0001)[10\underline{1}0]\|ZnO(0001)[10\underline{1}0]$ and Ni$(111)[112]\|$ZnO$(0001)[10\underline{1}0]$. This well ordered structure of NCs could result in a rather smooth interface between them and ZnO host and makes the hybrid of ferromagnetic NCs and semiconductors promising for spintronics functionality.

(3) Magnetic anisotropy is observed for Co or Ni NCs in ZnO. Especially for the Ni NCs, the anisotropy is different from the bulk crystals. The extra anisotropy energy is attributed to the lattice strain impressed from the host matrix. This opens a route to artificially tune the magnetic properties of nanoparticles by selecting substrate materials.

(4) The structure and magnetic properties of Co or Ni NCs embedded inside ZnO can be tuned by postannealing. For the Co case, 823 K annealing results in the coexistence of fcc-Co and hcp-Co. The magnetic anisotropy is changed from out of plane to in plane. Annealing at 923 K could have partially oxidized metallic Co and Ni and result in Co/CoO (Ni/NiO) core/shell structures. After annealing at 1073 K, no Co or Ni NCs can be detected within the detection limit of SR-XRD; at the same time, the samples shows no pronounced ferromagnetism down to 5 K.

*s.zhou@fzd.de

[1] H. Munekata, H. Ohno, S. von Molnar, A. Segmüller, L. L. Chang, and L. Esaki, Phys. Rev. Lett. **63**, 1849 (1989).
[2] H. Ohno, A. Shen, F. Matsukura, A. Oiwa, A. Endo, S. Katsumoto, and Y. Iye, Appl. Phys. Lett. **69**, 363 (1996).
[3] Y. Ohno, D. K. Young, B. Beschoten, F. Matsukura, H. Ohno, and D. D. Awschalom, Nature (London) **402**, 790 (1999).
[4] T. Jungwirth, K. Y. Wang, J. Mašek, K. W. Edmonds, J. König, J. Sinova, M. Polini, N. A. Goncharuk, A. H. MacDonald, M. Sawicki *et al.*, Phys. Rev. B **72**, 165204 (2005).
[5] T. Dietl, H. Ohno, F. Matsukura, J. Cibert, and D. Ferrand, Science **287**, 1019 (2000).
[6] K. Sato and H. Katayama-Yoshida, Physica E (Amsterdam) **10**, 251 (2001).
[7] B. Angadi, Y. S. Jung, W. K. Choi, R. Kumar, K. Jeong, S. W. Shin, J. H. Lee, J. H. Song, M. W. Khan, and J. P. Srivastava, Appl. Phys. Lett. **88**, 142502 (2006).
[8] Y. W. Heo, M. P. Ivill, K. Ip, D. P. Norton, S. J. Pearton, J. G. Kelly, R. Rairigh, A. F. Hebard, and T. Steiner, Appl. Phys. Lett. **84**, 2292 (2004).
[9] N. H. Hong, V. Brize, and J. Sakai, Appl. Phys. Lett. **86**, 082505 (2005).
[10] N. H. Hong, J. Sakai, and A. Hassini, J. Phys.: Condens. Matter **17**, 199 (2005).
[11] K. Ip, R. M. Frazier, Y. W. Heo, D. P. Norton, C. R. Abernathy, S. J. Pearton, J. Kelly, R. Rairigh, A. F. Hebard, J. M. Zavada *et al.*, J. Vac. Sci. Technol. B **21**, 1476 (2003).
[12] S. W. Jung, S. J. An, G. C. Yi, C. U. Jung, S. I. Lee, and S. Cho, Appl. Phys. Lett. **80**, 4561 (2002).
[13] A. Y. Polyakov, A. V. Govorkov, N. B. Smirnov, N. V. Pashkova,

S. J. Pearton, K. Ip, R. M. Frazier, C. R. Abernathy, D. P. Norton, J. M. Zavada *et al.*, Mater. Sci. Semicond. Process. **7**, 77 (2004).

[14] A. C. Tuan, J. D. Bryan, A. B. Pakhomov, V. Shutthanandan, S. Thevuthasan, D. E. McCready, D. Gaspar, M. H. Engelhard, J. W. Rogers, Jr., K. Krishnan *et al.*, Phys. Rev. B **70**, 054424 (2004).

[15] M. Venkatesan, C. B. Fitzgerald, J. G. Lunney, and J. M. D. Coey, Phys. Rev. Lett. **93**, 177206 (2004).

[16] S. J. Pearton, C. R. Abernathy, D. P. Norton, A. F. Hebard, Y. D. Park, L. A. Boatner, and J. D. Budai, Mater. Sci. Eng., R. **40**, 137 (2003).

[17] S. J. Pearton, D. P. Norton, K. Ip, Y. W. Heo, and T. Steiner, Prog. Mater. Sci. **50**, 293 (2005).

[18] S. J. Pearton, D. P. Norton, M. P. Ivill, A. F. Hebard, J. M. Zavada, W. M. Chen, and I. A. Buyanova, IEEE Trans. Electron Devices **54**, 1040 (2007).

[19] M. Bouloudenine, N. Viart, S. Colis, J. Kortus, and A. Dinia, Appl. Phys. Lett. **87**, 052501 (2005).

[20] S. Yin, M. X. Xu, L. Yang, J. F. Liu, H. Rösner, H. Hahn, H. Gleiter, D. Schild, S. Doyle, T. Liu *et al.*, Phys. Rev. B **73**, 224408 (2006).

[21] P. Sati, C. Deparis, C. Morhain, S. Schafer, and A. Stepanov, Phys. Rev. Lett. **98**, 137204 (2007).

[22] M. Fukumura, Z. W. Jin, M. Kawasaki, T. Shono, T. Hasegawa, S. Koshihara, and H. Koinuma, Appl. Phys. Lett. **78**, 958 (2001).

[23] Z. W. Jin, T. Fukumura, M. Kawasaki, K. Ando, H. Saito, T. Sekiguchi, Y. Z. Yoo, M. Murakami, Y. Matsumoto, T. Hasegawa *et al.*, Appl. Phys. Lett. **78**, 3824 (2001).

[24] C. N. R. Rao and F. L. Deepak, J. Mater. Chem. **15**, 573 (2005).

[25] Z. Zhang, Q. Chen, H. D. Lee, Y. Y. Xue, Y. Y. Sun, H. Chen, F. Chen, and W. K. Chu, J. Appl. Phys. **100**, 043909 (2006).

[26] S. Zhou, K. Potzger, H. Reuther, K. Kuepper, W. Skorupa, M. Helm, and J. Fassbender, J. Appl. Phys. **101**, 09H109 (2007).

[27] D. P. Norton, M. E. Overberg, S. J. Pearton, K. Pruessner, J. D. Budai, L. A. Boatner, M. F. Chisholm, J. S. Lee, Z. G. Khim, Y. D. Park *et al.*, Appl. Phys. Lett. **83**, 5488 (2003).

[28] K. Potzger, S. Q. Zhou, H. Reuther, A. Mücklich, F. Eichhorn, N. Schell, W. Skorupa, M. Helm, J. Fassbender, T. Herrmannsdorfer *et al.*, Appl. Phys. Lett. **88**, 052508 (2006).

[29] S. Zhou, K. Potzger, G. Zhang, F. Eichhorn, W. Skorupa, M. Helm, and J. Fassbender, J. Appl. Phys. **100**, 114304 (2006).

[30] S. Zhou, K. Potzger, H. Reuther, G. Talut, F. Eichhorn, J. von Borany, W. Skorupa, M. Helm, and J. Fassbender, J. Phys. D **40**, 964 (2007).

[31] S. Zhou, K. Potzger, G. Zhang, A. Mücklich, F. Eichhorn, N. Schell, R. Grotzschel, B. Schmidt, W. Skorupa, M. Helm *et al.*, Phys. Rev. B **75**, 085203 (2007).

[32] G. Talut, H. Reuther, A. Mücklich, F. Eichhorn, and K. Potzger, Appl. Phys. Lett. **89**, 161909 (2006).

[33] M. Jamet, A. Barski, T. Devillers, V. Poydenot, R. Dujardin, P. Bayle-Guillemaud, J. Rothman, E. Bellet-Amalric, A. Marty, J. Cibert *et al.*, Nat. Mater. **5**, 653 (2006).

[34] K. W. Liu, J. Y. Zhang, D. Z. Shen, X. J. Wu, B. H. Li, B. S. Li, Y. M. Lu, and X. W. Fan, Appl. Phys. Lett. **90**, 092507 (2007).

[35] T. Dietl and H. Ohno, Mater. Today **9**, 18 (2006).

[36] S. Kuroda, N. Nishizawa, K. Takita, M. Mitome, Y. Bando, K. Osuch, and T. Dietl, Nat. Mater. **6**, 440 (2007).

[37] S. R. Shinde, S. B. Ogale, J. S. Higgins, H. Zheng, A. J. Millis, V. N. Kulkarni, R. Ramesh, R. L. Greene, and T. Venkatesan, Phys. Rev. Lett. **92**, 166601 (2004).

[38] P. Sati, R. Hayn, R. Kuzian, S. Regnier, S. Schafer, A. Stepanov, C. Morhain, C. Deparis, M. Laugt, M. Goiran *et al.*, Phys. Rev. Lett. **96**, 017203 (2006).

[39] J. W. Lee, S. Kuroda, F. Takano, H. Akinaga, and K. Takita, Phys. Status Solidi C **3**, 4098 (2007).

[40] T. Fukumura, Y. Yamada, H. Toyosaki, T. Hasegawa, H. Koinuma, and M. Kawasaki, Appl. Surf. Sci. **223**, 62 (2004).

[41] C. Liu, F. Yun, and H. Morkoc, J. Mater. Sci.: Mater. Electron. **16**, 555 (2005).

[42] R. Seshadri, Curr. Opin. Solid State Mater. Sci. **9**, 1 (2005).

[43] J. Y. Kim, J. H. Park, B. G. Park, H. J. Noh, S. J. Oh, J. S. Yang, D. H. Kim, S. D. Bu, T. W. Noh, H. J. Lin *et al.*, Phys. Rev. Lett. **90**, 017401 (2003).

[44] J. Ziegler, J. Biersack, and U. Littmark, *The Stopping and Range of Ions in Matter* (Pergamon, New York, 1985).

[45] W. K. Chu, J. W. Mayer, and M. A. Nicolet, *Backscattering Spectrometry* (Academic, New York, 1978).

[46] S. O. Kucheyev, J. S. Williams, C. Jagadish, J. Zou, C. Evans, A. J. Nelson, and A. V. Hamza, Phys. Rev. B **67**, 094115 (2003).

[47] B. D. Cullity, *Elements of X-ray Diffractions* (Addison-Wesley, Reading, MA, 1978).

[48] M. Respaud, J. M. Broto, H. Rakoto, A. R. Fert, L. Thomas, B. Barbara, M. Verelst, E. Snoeck, P. Lecante, A. Mosset *et al.*, Phys. Rev. B **57**, 2925 (1998).

[49] F. Brem, L. Tiefenauer, A. Fink, J. Dobson, and A. M. Hirt, Phys. Rev. B **73**, 224427 (2006).

[50] G. M. Tsoi, L. E. Wenger, U. Senaratne, R. J. Tackett, E. C. Buc, R. Naik, P. P. Vaishnava, and V. Naik, Phys. Rev. B **72**, 014445 (2005).

[51] M. Farle, *Magnetism Goes Nano (Proceedings of the 36th IFF Spring School, Jülich, Germany, 2005)* (Research Center of Jülich, Jülich, Germany, 2005), p. C4.2.

[52] L. G. Jacobsohn, M. F. Hundley, J. D. Thompson, R. M. Dickerson, and M. Nastasi, J. Vac. Sci. Technol. B **24**, 321 (2006).

[53] K. Ando, A. Chiba, and H. Tanoue, Appl. Phys. Lett. **73**, 387 (1998).

[54] S. Zhou, K. Potzger, G. Talut, H. Reuther, J. von Borany, R. Grötzschel, W. Skorupa, M. Helm, J. Fassbender, N. Volbers, and M. Lorenz, J. Appl. Phys. **103**, 023902 (2008).

[55] V. M. Kaganer, O. Brandt, A. Trampert, and K. H. Ploog, Phys. Rev. B **72**, 045423 (2005).

[56] L. G. Jacobsohn, M. E. Hawley, D. W. Cooke, M. F. Hundley, J. D. Thompson, R. K. Schulze, and M. Nastasi, J. Appl. Phys. **96**, 4444 (2004).

[57] S. Shikazumi, *Physics of Ferromagnetism* (Oxford University Press, Oxford, 1997).

[58] A. Kumar, S. Fahler, H. Schlorb, K. Leistner, and L. Schultz, Phys. Rev. B **73**, 064421 (2006).

[59] O. Kazakova, B. Daly, and J. D. Holmes, Phys. Rev. B **74**, 184413 (2006).

[60] V. Skumryev, S. Stoyanov, Y. Zhang, G. Hadjipanayis, D. Givord, and J. Nogues, Nature (London) **423**, 850 (2003).

[61] A. N. Dobrynin, D. N. Ievlev, K. Temst, P. Lievens, J. Margueritat, J. Gonzalo, C. N. Afonso, S. Q. Zhou, A. Vantomme, E. Piscopiello *et al.*, Appl. Phys. Lett. **87**, 012501 (2005).